IEEE Access
Multidisciplinary ⋮ Rapid Review ⋮ Open Access Journal

Received March 17, 2021, accepted March 19, 2021, date of publication March 24, 2021, date of current version April 2, 2021.

Digital Object Identifier 10.1109/ACCESS.2021.3068400

Fat-IntraBody Communication at 5.8 GHz: Verification of Dynamic Body Movement Effects Using Computer Simulation and Experiments

NOOR BADARIAH ASAN[1,2], (Member, IEEE), EMADELDEEN HASSAN[3,4,5,6], MAURICIO DAVID PEREZ[1], (Member, IEEE), LAYA JOSEPH[1], MARTIN BERGGREN[7], THIEMO VOIGT[8], (Member, IEEE), AND ROBIN AUGUSTINE[1], (Member, IEEE)

[1]Ångström Laboratory, Microwaves in Medical Engineering Group, Department of Electrical Engineering, Uppsala University, 75121 Uppsala, Sweden
[2]Centre for Telecommunication Research and Innovation (CeTRI), Fakulti Kejuruteraan Elektronik dan Kejuruteraan Komputer, Universiti Teknikal Malaysia Melaka, Durian Tunggal 76100, Malaysia
[3]Department of Applied Physics and Electronics, Umeå University, 901 87 Umeå, Sweden
[4]Department of Electronics and Electrical Communications, Menoufia University, Menouf 32952, Egypt
[5]Hannover Centre for Optical Technologies, Cluster of Excellence PhoenixD, Leibniz University Hannover, 30167 Hanover, Germany
[6]Faculty of Mechanical Engineering, Institute of Transport and Automation Technology, Leibniz University Hannover, 30823 Garbsen, Germany
[7]Department of Computing Science, Umeå University, 901 87 Umeå, Sweden
[8]Department of Information Technology, Uppsala University, 752 36 Uppsala, Sweden

Corresponding authors: Noor Badariah Asan (noorbadariah@utem.edu.my) and Robin Augustine (robin.augustine@angstrom.uu.se)

This work was supported in part by the Ministry of Higher Education Malaysia, in part by the Universiti Teknikal Malaysia Melaka, in part by the Swedish Foundation for Strategic Research Lifesec: Don't Hack My Body! Project under Grant RIT17-0020 and the ZeroIoT: Enabling the Battery-Free Internet of Things under Grant CHI19-0003, in part by the H2020EU Project (Soft Intelligence Epidermal Communication Platform) under Grant SINTEC-824984, in part by the eSSENCE, a Strategic Collaborative eScience Program funded by the Swedish Research Council, and in part by the Eurostars Project E!114232-MAS-Muscle Analysis System.

ABSTRACT This paper presents numerical modeling and experimental validation of the signal path loss at the 5.8 GHz Industrial, Scientific, and Medical (ISM) band, performed in the context of fat-intrabody communication (fat-IBC), a novel intrabody communication platform using the body-omnipresent fat tissue as the key wave-guiding medium. Such work extends our previous works at 2.0 and 2.4 GHz in the characterization of its performance in other useful frequency range. In addition, this paper also includes studies of both static and dynamic human body movements. In order to provide with a more comprehensive characterization of the communication performance at this frequency, this work focuses on investigating the path loss at different configurations of fat tissue thickness, antenna polarizations, and locations in the fat channel. We bring more realism to the experimental validation by using excised tissues from porcine cadaver as both their fat and muscle tissues have electromagnetic characteristics similar to those of human with respect to current state-of-art artificial phantom models. Moreover, for favorable signal excitation and reception in the fat-IBC model, we used topology optimized waveguide probes. These probes provide an almost flat response in the frequency range from 3.2 to 7.1 GHz which is higher than previous probes and improve the evaluation of the performance of the fat-IBC model. We also discuss various aspects of real-world scenarios by examining different models, particularly homogeneous multilayered skin, fat, and muscle tissue. To study the effect of dynamic body movements, we examine the impact of misalignment, both in space and in wave polarization, between implanted nodes. We show in particular that the use of fat-IBC techniques can be extended up in frequency to a broadband channel at 5.8 GHz.

INDEX TERMS Channel characterization, dielectric properties measurement, ex-vivo, fat tissue, fat-IBC, intrabody microwave communication; ISM band, path loss, polarization, topology optimization.

I. INTRODUCTION

In-vivo smart implants operate in Industrial, Scientific, and Medical (ISM) bands. According to the U.S. Food Drug Administration (FDA) [1], the frequency 5.8 GHz, together with the frequencies 433 MHz, 900 MHz, and 2.4 GHz, which belong to the ISM band, are recognized as frequencies that can be utilized for active implantable medical devices, such as cardiac pacemakers, cardioverter defibrillators, and cardiac resynchronization devices [2]. The ISM frequencies at

The associate editor coordinating the review of this manuscript and approving it for publication was Shah Nawaz Burokur.

2.4 GHz or 5.8 GHz are typically chosen for in-body implants as a compromise between small antenna size (higher frequencies allow smaller antennas) and acceptable penetration through human body tissues, although at lower frequencies the penetration is higher [3]. One main challenge for in-body implants is the miniaturization of the antenna. Because of the lossy nature of biological tissues, higher-frequency waves attenuate faster than lower-frequency waves, and therefore reduce the communication range. Numerous implantable systems are currently available in the market, including drug delivery systems [4]–[6], cochlear implants [7], [8], pressure monitors in the brain [9]–[11], glaucoma sensors [12], [13], and direct control of prostheses [14]–[16]. By including the wireless technology in their market offers, the use of such systems is enormously extended. This trend is also widely noticed in the literature through the increasing interest in miniature antennas for implants [17]–[21].

In previous studies at lower microwave frequencies (2.0 and 2.4 GHz) [22]–[24], the path loss of fat-intrabody communication (fat-IBC) has been investigated against different factors that might affect the signal path loss. These studies show that the path loss depends on several properties of the fat tissue. When there are perturbants or muscles that correspond to a height greater than 40% of the fat's thickness, the path loss increases significantly [25], while for the physical curvature variation of fat tissue, a loss of 4 dB is expected in extreme scenarios [26]. Blood vessels in fat tissue cause a path loss that depends on their position and orientation in the fat tissue; they can behave as a reflector, a splitter, or as a splitter and re-combiner [27]. Recent studies report on the effect of steel wires, placed in human chest in the context of open-heart surgeries, on microwave intrabody communication [28]. Särestöniemi *et al.* discuss intrabody channel characteristics between a capsule endoscope and a receiving directive on-body antenna at UWB frequencies for wireless body-area networks [29]. Inspired by the insights gained from these previous studies and the value of considering operations at higher frequencies, in this work we investigate fat-IBC at 5.8 GHz using numerical simulations and laboratory experiments using porcine cadaver tissues to enhance realism.

Moreover, we propose a small probe optimized to operate efficiently into the fat tissue at a frequency of 5.8 GHz. The small size of the probe, together with the experiment setup, makes it possible to investigate new aspects of this intrabody communication. In particular, the small size allows the study of intrabody communication subject to dynamic body movements where the position of implanted nodes are likely to be displaced. The displacement of nodes can change the relative orientation and position between nodes as well as their respective polarization, affecting the quality of the channel. These investigations have the potential to provide valuable information that can be utilized in designing reliable communication between implants, particularly for fat-IBC. Table 1 shows the difference in probe size between some previous work at 2.0 GHz and 2.4 GHz and the current work.

TABLE 1. Comparison between the waveguide probe sizes at 2.0 GHz, 2.4 GHz, and 5.8 GHz (current work).

Work	Waveguide section ($W \times T \times L$) mm^3	Frequency range (GHz)	Design frequency (GHz)
[22]	$25 \times 50.5 \times 70$	1.9–2.1	2.0
[23]	$25.4 \times 50.7 \times 60.9$	1.6–2.7	2.4–2.45
Proposed	$9.9 \times 19.1 \times 14.3$	4.9–7.05	5.8

The novelty of the research is that the use of fat-IBC techniques can be extended up in frequency to a broadband channel at 5.8 GHz. We study the effect of dynamic body movements by examining the impact of misalignment, both in space and in wave polarization, between implanted nodes. Moreover, another novel aspect of this paper is the development of a simplified generic path loss (PL) model, which describes the signal attenuation between a transmitter (TX) and a receiver (RX) antenna as a function of the propagation distance at 5.8 GHz. We select the 5.8 GHz frequency corresponding to the ISM band, as this choice is one way to reduce the antenna size and to make the antenna feasible for implantation. Another advantage of this choice is the wide bandwidth offered by operating at 5.8 GHz, which enables high data rates that could be utilized, for instance, for live streaming of gastro-intestinal video signals.

The paper is organized as follows. Section 2 describes the dielectric properties of the ex-vivo tissues and a proposed phantom model used in the laboratory and compared to the human tissue. The description of the topology optimized probes, along with the measurement setup of the probes, is given in Section 3. In Section 4, we describe the experimental setup for a set of possible configurations for the fat channel and different alignments between the probes. Section 5 presents numerical and experimental results that demonstrate the benefit of our new investigation of the fat channel at 5.8 GHz. The conclusion is given in Section 6.

II. DIELECTRIC PROPERTIES OF THE TISSUE-EQUIVALENT PHANTOM, EX-VIVO, AND HUMAN TISSUES

In this study, we perform experiments in two environments—tissue-equivalent phantom and ex-vivo tissue—and compare with the human tissue developed by Andreuccetti *et al.* [30], based on the work of Gabriel *et al.* [31], [32]. Tissue-equivalent phantoms emulating skin and muscle were made as agar-based compounds, while those emulating fat were made as oil-based compounds. The phantoms used in this work were developed in our laboratory using recipes similarly as done in Joseph *et al.* [33]. For the ex-vivo tissues, the skin, fat, and muscle were separated from the porcine belly portion obtained from a local slaughterhouse. The fat and muscle have been finely minced with a meat mincer to reduce air traps between the two layers when forming the model structure.

To establish suitable models to study fat-IBC, the frequency-dependent, real ε' and imaginary ε'', parts of the dielectric permittivity of the skin, fat, and muscle

tissues are determined. We measure these quantities using a Keysight N1501A open-ended dielectric slim form probe kit. For numerical simulations, Cole-Cole models are used to fit the measured data. Figure 1 shows a comparison between the dielectric properties, over the frequency range 3–8 GHz, of the three models: (i) freshly excised ex-vivo porcine belly tissues, (ii) tissue-equivalent phantom compounds, and (iii) human tissues. From Figure 1a we can see that the dielectric constant ε' of the ex-vivo skin tissue is slightly lower than that of the human skin. However, we could consider them to be statistically similar, as the reported uncertainty in the Keysight N1510A dielectric probe system is about 10% [34], mainly at lower frequencies, and as they are tissues of different nature. Moreover, the uncertainties from the data in the IFAC database, Andreuccetti *et al.* [30], could be considered in the worst-case scenario as much as 10%, according to the work by Gabriel and Peyman [35].

Figure 1b presents the dielectric properties of the fat tissue as a function of frequency. It shows that the dielectric properties of an ex-vivo fat tissue are similar to the human fat tissue. The dielectric constant, ε' of the oil-based phantom is also similar above 5 GHz, but ε'' is twice the value of ex-vivo and human tissue. This is a drawback of the phantom recipe that was employed to ensure a flexible phantom that could be used in experimental scenarios where the phantom needs to be bended. Further, this phantom is used to study the behaviour of the fat channels possessing different electromagnetic properties. The muscle tissues of the phantom and ex-vivo have smaller ε'' compared with those of the human tissue, whereas their ε' have slightly higher values than those of the human tissue (see Figure 1c). Therefore, these values can be used in our experiments.

Table 2 shows the comparison of the dielectric properties extracted at 5.8 GHz ISM band from Figure 1. Since the fat tissue has a lower loss tangent tan δ, and since waves in this medium travel faster than in the muscle and skin tissues, a wave travelling through the fat will experience a lower path loss than in other tissues. It can be seen that the ex-vivo porcine fat tissue has similar characteristics as the human tissue, while the phantom has twice their loss tangent.

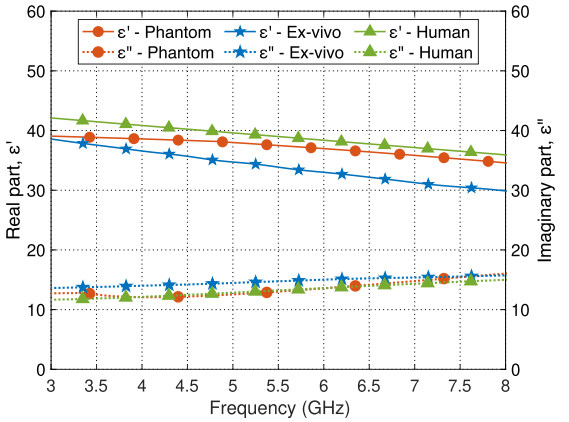

(a) Dielectric properties (ε' and ε") of skin as a function of frequency (3–8 GHz).

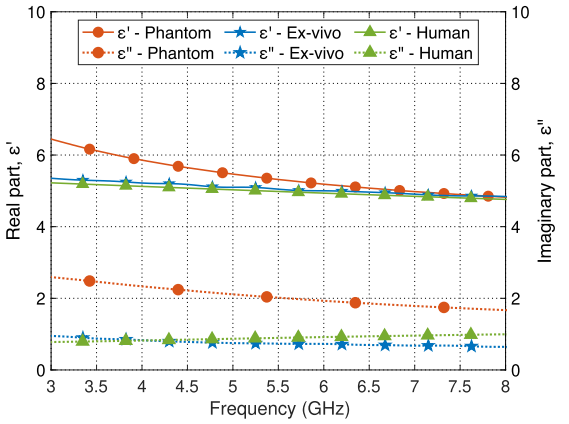

(b) Dielectric properties (ε' and ε") of fat as a function of frequency (3–8 GHz).

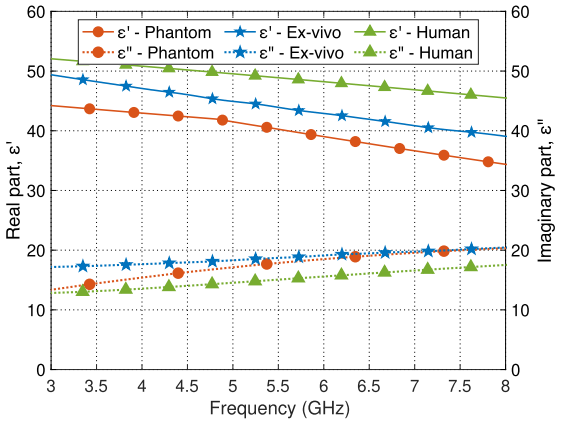

(c) Dielectric properties (ε' and ε") of muscle as a function of frequency (3–8 GHz).

FIGURE 1. A comparison between the complex dielectric properties of the tissue-equivalent phantom, the ex-vivo tissues, and the human tissues at room temperature.

III. TOPOLOGY OPTIMIZED COMPACT PROBE

A. PROBE OPTIMIZATION

To investigate the fat channel communication at 5.8 GHz, we need to efficiently launch and record electromagnetic waves into and from the fat tissue. To achieve this goal, we design a wideband probe by using our topology optimization approach [36]. Figure 2 shows the configuration of the proposed probe, consisting of a coaxial cable connected to one side of a rectangular cavity with dimensions $W_{\text{probe}} = 19.05\,\text{mm}$ $T_{\text{probe}} = 9.525\,\text{mm}$ and $L_{\text{probe}} = 14.3\,\text{mm}$. The cavity region is filled with a substance having permittivity properties similar to that of the fat tissue. The opposite side of the cavity is open towards the fat tissue domain Ω_{ex} and represents a radiating aperture with a size of $W_{\text{probe}} \times T_{\text{probe}}$. The aperture size is similar to the dimensions of a standard WR75 waveguide, which allows the use of WR75 waveguide sections for the probe assembly. Outside the cavity, the domain Ω_{ex} has a wave impedance that depends on the

TABLE 2. Comparison between the dielectric properties of the tissue-equivalent phantom, ex-vivo porcine tissue, and human tissue at 5.8 GHz.

Tissue	Parameter	Ex-vivo	*Phantom*	Human [30]
Skin	Conductivity, σ	4.8 ± 0.5	4.6 ± 0.5	3.7 ± 0.2
	Relative permittivity, ε'	33 ± 3	41 ± 4	35 ± 2
	Loss tangent, tan δ	0.45 ± 0.04	0.36 ± 0.04	0.33 ± 0.02
Fat	Conductivity, σ	0.2 ± 0.02	0.6 ± 0.06	0.3 ± 0.01
	Relative permittivity, ε'	5.0 ± 0.5	5.2 ± 0.5	5.0 ± 0.2
	Loss tangent, tan δ	0.15 ± 0.01	0.37 ± 0.04	0.18 ± 0.01
Muscle	Conductivity, σ	6.1 ± 0.6	6.0 ± 0.6	5.0 ± 0.2
	Relative permittivity, ε'	43 ± 4	39 ± 4	48 ± 2
	Loss tangent, tan δ	0.44 ± 0.04	0.48 ± 0.05	0.32 ± 0.02

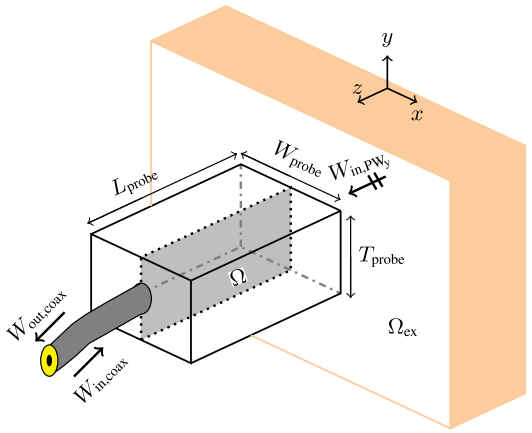

FIGURE 2. Configuration of the probe and its attachment to the exterior domain Ω_{ex}. The domain Ω is the design domain where the conductivity distribution is optimized to maximize signal transmission between the probe and Ω_{ex}.

complex permittivity of the medium. Here, domain Ω_{ex} is assumed to possess the complex permittivity of the fat tissue. Note that the matching between the probe and Ω_{ex} depends on the probe's geometrical parameters, the material property inside the probe, and the wave impedance of the exterior domain, as will be demonstrated next.

To design the probe, we formulate the conceptual optimization problem

$$\begin{cases} \max_{\sigma_\Omega} \log\left(\dfrac{\boldsymbol{W}_{\text{out,coax}}|\boldsymbol{W}_{\text{PWy}}}{\boldsymbol{W}_{\text{out,coax}}|\boldsymbol{W}_{\text{in,coax}}}\right), \\ \text{subject to governing equations and excitation signals} \end{cases} \tag{1}$$

where σ_Ω is the conductivity distribution in the planar domain Ω, located at the middle of the cavity; $\boldsymbol{W}_{\text{out,coax}}|\boldsymbol{W}_{\text{PWy}}$ is the received energy in the coaxial cable when a y-polarized plane wave propagates from Ω_{ex} towards the probe; and $\boldsymbol{W}_{\text{out,coax}}|\boldsymbol{W}_{\text{in,coax}}$ is the reflected energy to the coaxial cable when the coaxial cable is the source of transmission. Problem (1) reads: find the conductivity distribution in Ω that (i) maximizes the energy received by the probe $\boldsymbol{W}_{\text{out,coax}}|\boldsymbol{W}_{\text{PWy}}$ when the probe operates in the receiving mode and, at the same time, (ii) minimizes the energy reflected by the probe $\boldsymbol{W}_{\text{out,coax}}|\boldsymbol{W}_{\text{in,coax}}$ when the probe operates in the transmission mode.

We solve problem (1) using gradient-based optimization. The finite-difference time-domain (FDTD) method [37] in an in-house developed software numerically solves Maxwell's equations to compute the two factors of the objective functions. We use a uniform FDTD grid with a spatial step size $\Delta = 0.10583$ mm, and a temporal step size Δt equals 0.9 of the Courant stability limit, and 10 cells of a uniaxial perfectly matched layer (UPML) to truncate the simulation domain in all directions. The Coaxial cable port is simulated using the model presented in our previous work [38]. The domain Ω is pixelated into 90×135 Yee cells containing 24 525 edges. The vector of design variables holds the conductivity value at each edge in Ω. The gradient of the objective function is computed by an expression involving FDTD solutions of the governing Maxwell equations together with an adjoint system of equations associated with the current objective function [39]. The frequency band of interest is 3.6–7.2 GHz, which is determined by controlling the frequency spectrum of the excitation signals. The vector of design conductivities is updated iteratively by the globally convergent method of moving asymptotes (GCMMA) [40]. The GCMMA is a gradient-based optimization method particularly suitable for large-scale topology optimization problems. More details about the numerical treatments of problem (1) are presented in previous work [36], [41].

Figure 3 shows the development of the objective function and the design in Ω versus iteration number. The optimization algorithm converged after 156 iterations to the design shown in the inset of Figure 3. The black and white colors indicates copper and dielectric, respectively. We emphasize the large scale of the optimization problem: each pixel in the final design is a design variable, and there are 24 525 pixels. We present the design as an image with its axes scaled in millimeters to facilitate design reproducibility.

B. DESIGN AND FABRICATION OF THE PROBES

A prototype of the optimized probes is designed, developed, and fabricated. The probe consists of four elements: A rectangular waveguide section, a 50 Ω SubMiniature version A (SMA) connector, a topology optimized planar antenna, and a dielectric filling with a similar permittivity as the fat tissue. Figure 4 shows the prototype of the fabricated probe with the topology optimized planar antenna immersed inside

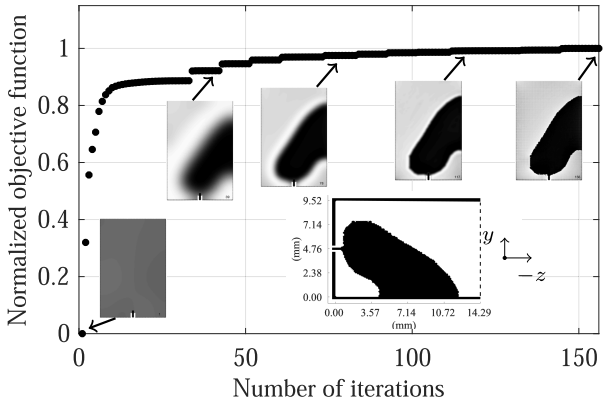

FIGURE 3. The development of the objective function and the design versus the number of iterations. The final design, shown as the inset, is plotted as an image with its axes scaled in millimeters for reproducibility. Black is copper and white is a dielectric.

the fat-equivalent phantom material. Three-dimensional (3D) perspective view of the probe is shown in Figure 4a. The topology optimized planar antenna (TOPA) is printed on a single-layer printed circuit board with a size of only 14.29 mm × 9.52 mm (see Figure 4b). The copper plate material is soldered in one side to the broad wall of the waveguide section. The TOPA was fabricated using 0.64 mm thick Rogers TMM6 substrate with dielectric constant ε' of 6 ± 0.08, loss tangent tan δ of 0.0023, and 0.035 mm copper thickness (see Figure 4c).

The performance of the optimized probe is analyzed by our in-house finite-difference time-domain (FDTD) code and cross-verified using the commercial CST Microwave Studio software package. We use the transient CST solver which employs the finite integration technique to numerically solve the electromagnetic governing equations [42]. As discussed in Section III-A, the performance of the probe depends on the properties of the surrounding medium. Here, we demonstrate this fact by comparing the performance of the probe when it radiates into different environments. The probe's performance is investigated based on computing the reflection coefficient when the probe is attached to the phantom-equivalent fat tissue (the medium for which the probe is optimized) and when it radiates into free-space (for which the probe is *not* optimized). Figure 5 shows the simulated reflection coefficient of the probe in both environments for comparison. When the probe is attached to the fat tissue, the $|S_{11}|$ is lower than –12 dB over the frequency range of 3.2–7.1 GHz, which contains the entire F-band frequencies of 4.9–7.05 GHz. These results show that the probe indeed has an excellent match with the fat tissue at 5.8 GHz. However, the $|S_{11}|$ is essentially above –5 dB when the probe radiates into free space. This increase in $|S_{11}|$ indicates that more energy is reflected back to the source. That is, the probe's performance deteriorates if it radiates into a medium different from what it was optimized for. The wideband performance of the optimized probe can be used to investigate the performance of the fat tissue at neighboring frequencies as well. We emphasize

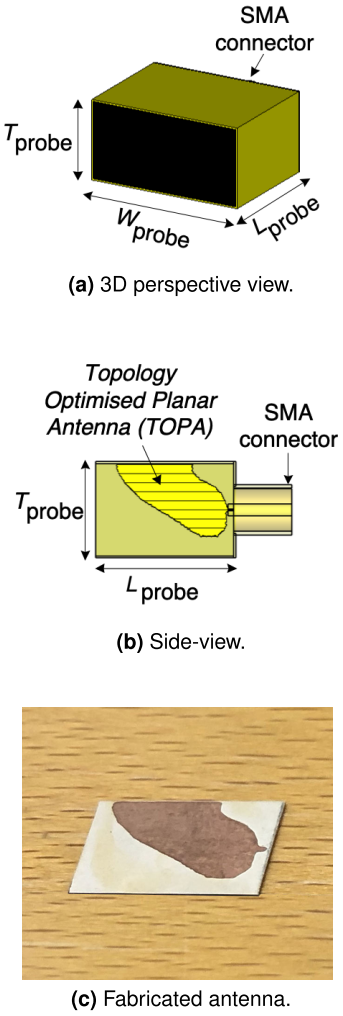

(a) 3D perspective view.

(b) Side-view.

(c) Fabricated antenna.

FIGURE 4. Probe dimensions and the topology optimized planar antenna.

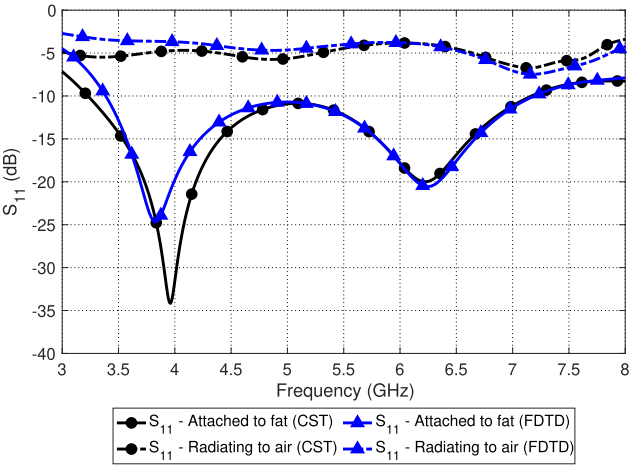

FIGURE 5. Amplitude of the probe's reflection coefficient $|S_{11}|$ when attached to radiate into the fat and free-space environment.

that our probe is used only to characterize the intrabody fat communication. For in-body or on-body communication, antennas with other objectives and constraints are typically needed [43], [44].

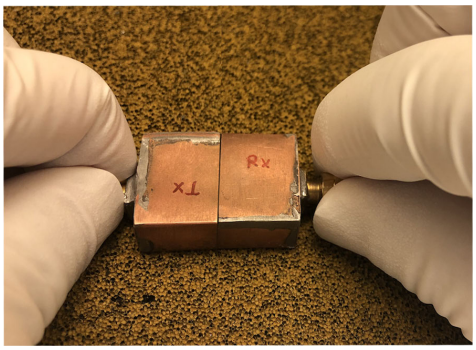

FIGURE 6. The probe to probe measurement setups.

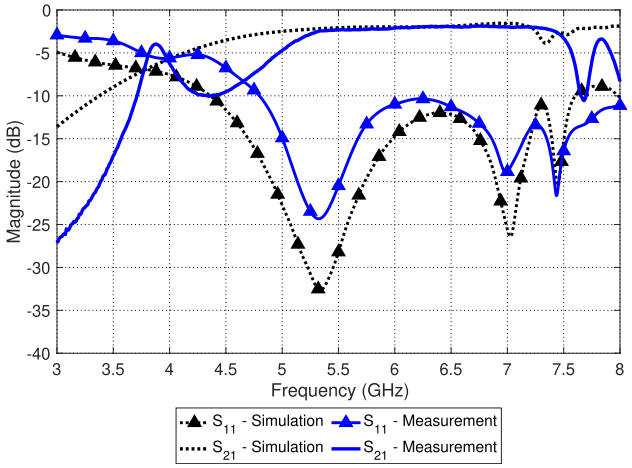

FIGURE 7. Scattering parameters of the probe-to-probe setup.

C. PROBE-TO-PROBE MEASUREMENTS AND RESULTS

Figure 6 shows the probe-to-probe measurement setup. The two probes, acting as a transmitter (TX) and a receiver (RX), are in contact with each other. The TX is connected to Port 1 and the RX to Port 2 of the microwave analyzer. The scattering parameters of the probes were measured using the Keysight Microwave FieldFox Analyzer (N9918A) [45] in the 3–8 GHz frequency range with data acquired at 1001 frequency points. A microwave absorber has been used to reduce the interaction between the probes and the surrounding environment.

Figure 7 shows the probe-to-probe simulated and measured scattering parameters. The simulated and measured coupling coefficients $|S_{21}|$ of the probe-to-probe setup are –2.0 dB and –2.2 dB, respectively, at 5.8 GHz. The probes show a reflection coefficient $|S_{11}|$ below –10 dB over the frequency range 4.4–8.0 GHz and 4.7–8.0 GHz for simulations and measurements, respectively. The small differences between the simulation and measurement results can be ascribed to air gaps in the dielectric material inside the probes as well as air gaps between the two probes. Figure 8 shows the Voltage Standing Wave Ratio (VSWR) of the probes. As we can see, the VSWR is below two at the frequency range of 4.3–8.0 GHz for simulation and 4.8–8.0 GHz for the measurement. These results confirm that the proposed probes are matched to the fat tissue, and that they contribute insertion

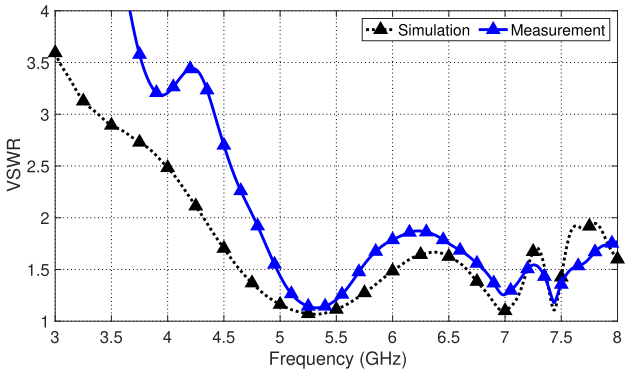

FIGURE 8. Measured and simulated voltage standing wave ratios for the probe-to-probe setup.

losses of 2.0 dB and 2.2 dB when the channel path loss is evaluated in simulation and measurement, respectively.

IV. CHARACTERIZATION OF THE FAT-IBC AT 5.8 GHz

A. EXPERIMENTAL SETUP

A comprehensive setup has been modeled, designed, and developed to characterize the fat-IBC at 5.8 GHz ISM band. In this section, four different configurations, Type A, Type B, Type C, and Type D of the three-layered tissue model structure, are proposed and discussed. All measurements are conducted in two different environments, tissue-equivalent phantom, and ex-vivo porcine tissue. In addition, we use the CST software to simulate these environments. The illustration of each type is shown in Figure 9. The thickness of skin and muscle tissue are fixed in all cases to 2 mm and 30 mm, respectively.

The thicknesses were chosen based on our previous work and they also present the average thickness of these tissue layers [22], [23], [46], [47]. The fat in this context is the tissue that is utilized for the fat-IBC characterization and is varied in two parameters, the thickness and the width. The thickness is changed from $T_{\text{fat}} = 9.93$ mm to $T_{\text{fat\_extend}} = 25$ mm, and the width is changed from $W = 19.10$ mm to $W_{\text{extend}} = 50$ mm. The channel length, L is varied from 20 mm to 100 mm in 20 mm steps.

In Type A, the channel is characterized by having the same L, W, and T_{fat} according to the dimension of the probes (see Figure 9a). In Type B, the width of the channel is extended by $W_{\text{extend}} = 50$ mm, while the other parameters remain the same as in Type A (see Figure 9b). Instead of having extra width, the fat thickness is extended in Type C, while the fat width remains the same as Type A (see Figure 9c). In Type D, we extend both the thickness and width of the fat channel (see Figure 9d). Figure 10 shows the setup for the Type D model when one of the probes is rotated by 90° in the fat tissue with a 100 mm channel length. The purpose of the latter setup is to observe the signal transmission and analyze the impact of changing the wave polarization on fat-IBC. Overall, the primary purpose of these experiments is to obtain a generic insight on how the path loss characteristics change under different conditions, as well as to understand

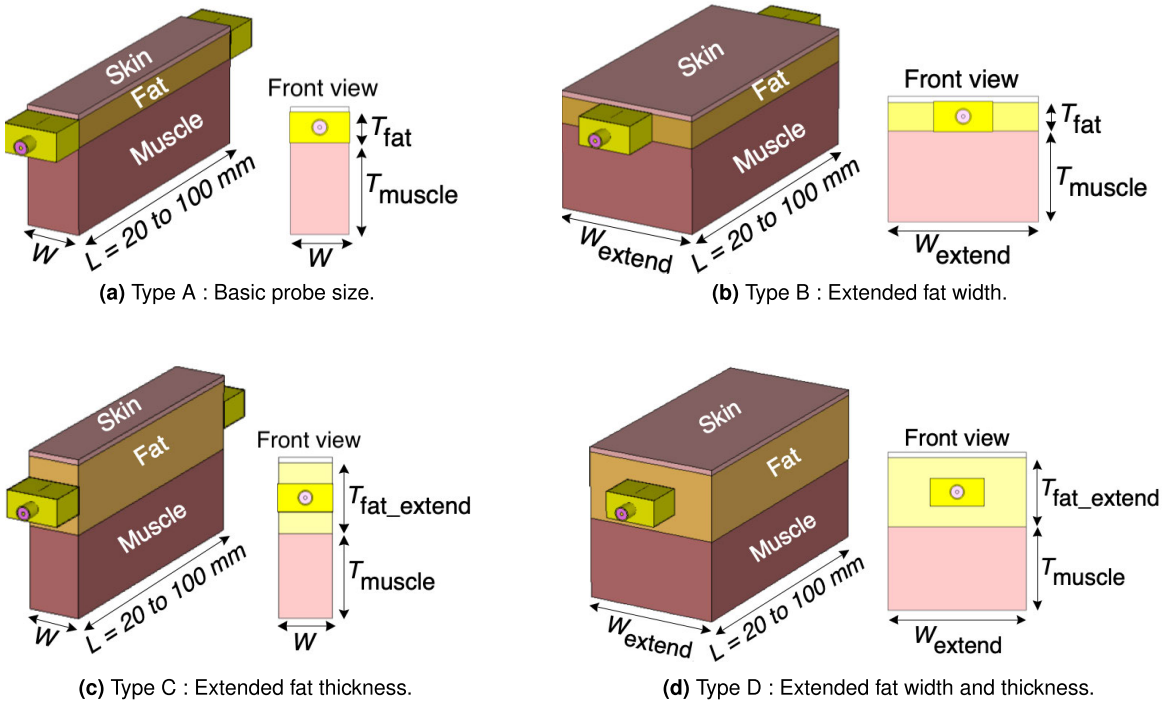

(a) Type A : Basic probe size.

(b) Type B : Extended fat width.

(c) Type C : Extended fat thickness.

(d) Type D : Extended fat width and thickness.

FIGURE 9. Four configurations of three-layered tissue model structure to characterize fat-IBC performance both numerically and experimentally.

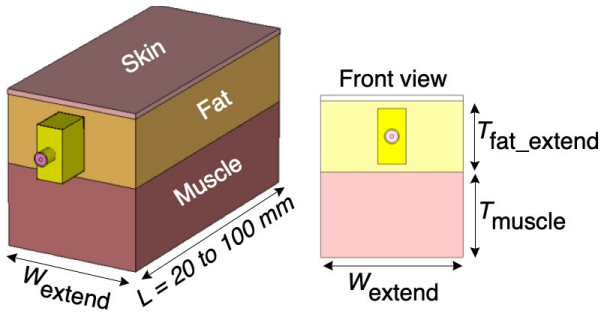

FIGURE 10. The model shows 90° rotated probe in the fat tissue. The setup is taken from Type D to characterize the impact of wave polarization fat-IBC.

the influence of the misalignment, in space or polarization, between the transmitting and receiving probes (nodes).

The experimental setups of the tissue-equivalent phantom and the ex-vivo tissue environment are shown in Figure 11. The phantom and ex-vivo tissues were kept at room temperature in the laboratory at 22 °C (71.6 °F) for at least 30 minutes to equalize their temperature to the room temperature. The experiments are done in room temperature in order to obtain reliable data and to ensure repeatability. The reference cadaver tissue data has been collected at room temperature and our experimental setup complies with the reported values in [48]. Even though the phantom and ex-vivo tissues were stabilized to room temperature, they may still differ in temperature with respect to the human data reported in [48] since the data obtained at temperature as low as 20 °C.

As shown in Figure 11a, the setup consists of a pair of rectangular probes, a Keysight Microwave FieldFox analyzer (N9918A), a coaxial cable connector, and a three-layered skin, fat, and muscle of ex-vivo porcine tissue (see Figure 11b) or phantom (see Figure 11c). The probes and ex-vivo tissue are supported by a 3D printed holder molded from polylactic acid (PLA) plastic material, which has the dielectric properties of 2.6 ± 0.2 in order to provide a stable fixture during the experiment. The frequency range of the measurements is 3–8 GHz. For each reading, we record the scattering parameters based on the average of five measurements.

B. NUMERICAL MODELING SETUP

We study numerically the effect on fat-IBC of misalignment between the probes (nodes) and the change in the wave polarization. We use the CST transient solver to simulate these environments. The simulation models are assigned with the respective dielectric properties of the constituent materials measured during the experiments. A fourth-order polynomial is used to fit the dielectric properties of the measured material data to the simulation model in CST. In our numerical model, we assume a free space medium above the skin layer, and we use a radiation boundary condition to surround the model in all sides to avoid reflections from the boundaries. First, to study the impact on the signal coupling with respect to the alignment, we change the positions of the transmitting and receiving probes vertically as well as horizontally inside the fat channel. We mark the center of the channel as the reference position.

Figure 12 shows a model consisting of two probes acting as transmitter (TX) and receiver (RX) that have been implanted

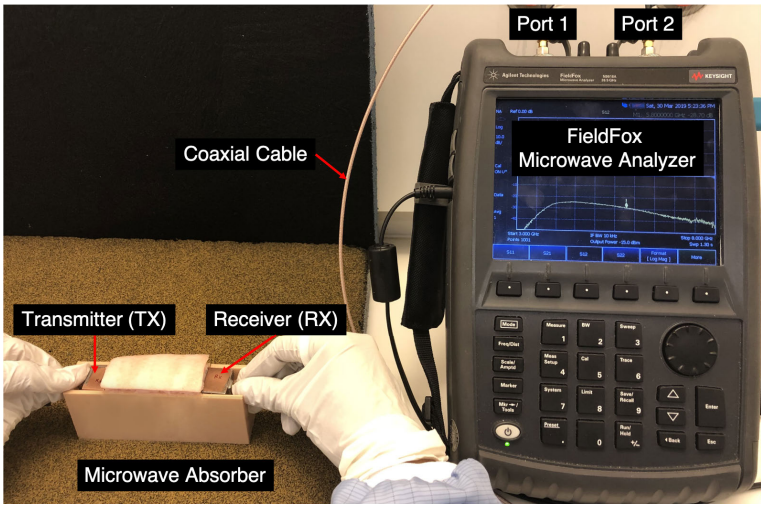

(a) Experimental setup.

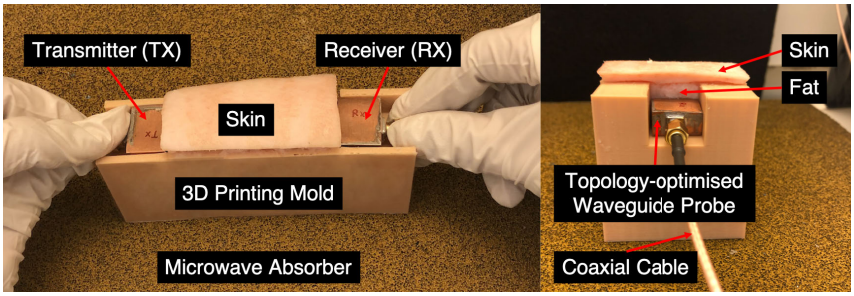

(b) Ex-vivo measurement.

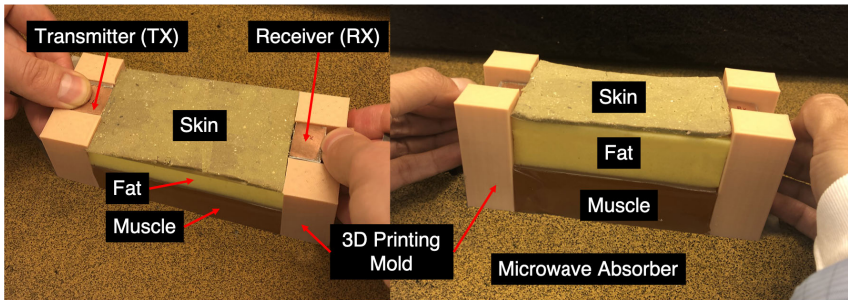

(c) Phantom measurement.

FIGURE 11. The measurement setup for tissue-equivalent phantom and ex-vivo porcine tissue.

in the fat tissue of the three-layered homogeneous tissue structure. The transmitter probe is aligned at four orientations: Up, Down, Left, and Right (see Figure 12a). Figure 12b shows one example where the transmitter is placed on top of the muscle tissue, and the receiver is situated at the center of the fat tissue. Second, we study the impact using a horizontal polarized electric field inside the fat channel. Compared to our previous probes [22], [23], the compact size of the new probes makes it feasible to investigate the use of a horizontally polarized electric field inside the fat channel. To do so, we rotate both the transmitting probe and the receiving probe by 90 degrees inside the fat channel.

The width and the length of the entire tissue are 80 mm $\times$ 180 mm, and the distance between the probes is fixed at 100 mm. The thicknesses of the skin, fat, and muscle are 2 mm, 25 mm, and 30 mm, respectively. The aim of the study is to observe the impact on the signal coupling with respect to the misalignment of the probes in the fat tissue, which helps to investigate the influence of misalignment between implant devices.

V. RESULTS AND DISCUSSION

A. CHANNEL PATH LOSS AT 5.8 GHz

Following the procedure in Section IV-A, we measured and computed the transmission coefficient $|S_{21}|$ as indicated in Figures 13–16, where the results of the ex-vivo porcine tissue environment and the tissue-equivalent phantom environment are presented in the left and right graphs,

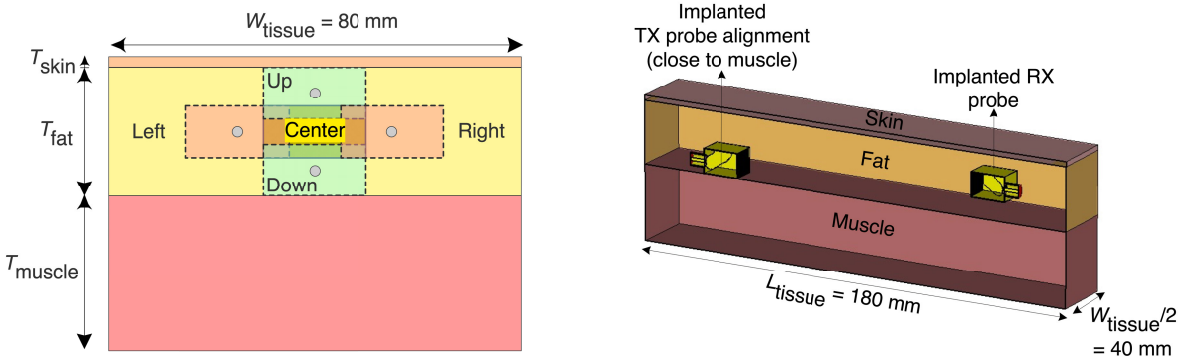

(a) Cross-view shows different misalignment scenarios between the probes. **(b)** Example of a misalignment.

FIGURE 12. **(a) Illustration of different alignment scenarios of the probes, where the transmitting (TX) probe is placed below the skin (Up), on top of the muscle tissue (Down), 15 mm to the left-side (Left), 15 mm to the right-side of the channel (Right), and at the center of the fat tissue (Center). (b) One example showing the TX probe placed on top of the muscle, while the RX probe remains at the center of the fat tissue.**

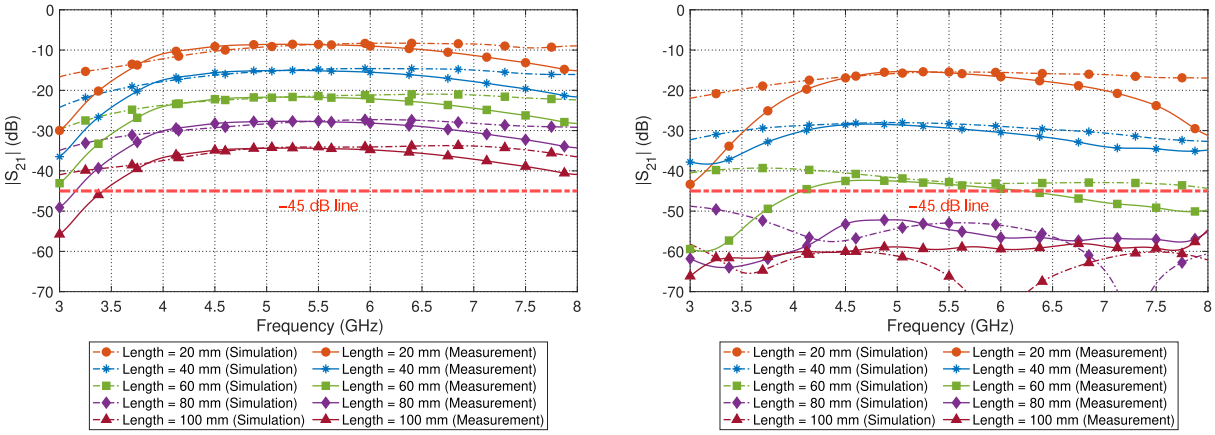

(a) Ex-vivo porcine tissue. **(b)** Tissue-equivalent phantom.

FIGURE 13. **Type A: Transmission coefficient, $|S_{21}|$ dB.**

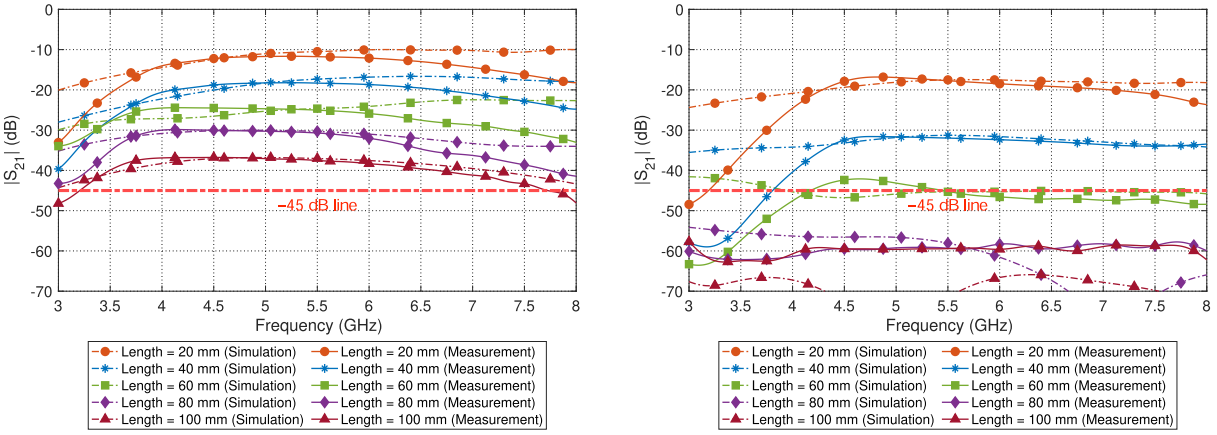

(a) Ex-vivo porcine tissue. **(b)** Tissue-equivalent phantom.

FIGURE 14. **Type B: Transmission coefficient, $|S_{21}|$ dB.**

respectively. The solid curves indicate the average of the $|S_{21}|$ measurements, while the dashed-dotted curves show the simulation results. We change the channel length from 20 mm to 100 mm for each case. Note that the loss tangent of the fat-equivalent phantom is almost twice the corresponding values of the human and ex-vivo fat tissues. Nevertheless, this fat-equivalent phantom can be used to facilitate the investigations of worst-case scenarios of the channel path loss.

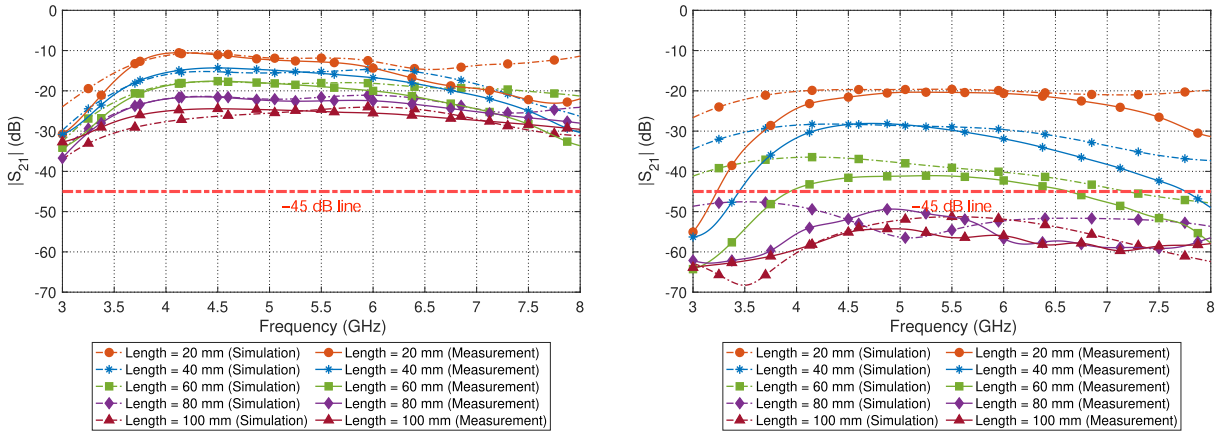

(a) Ex-vivo porcine tissue. **(b)** Tissue-equivalent phantom.

FIGURE 15. Type C: Transmission coefficient, $|S_{21}|$ dB.

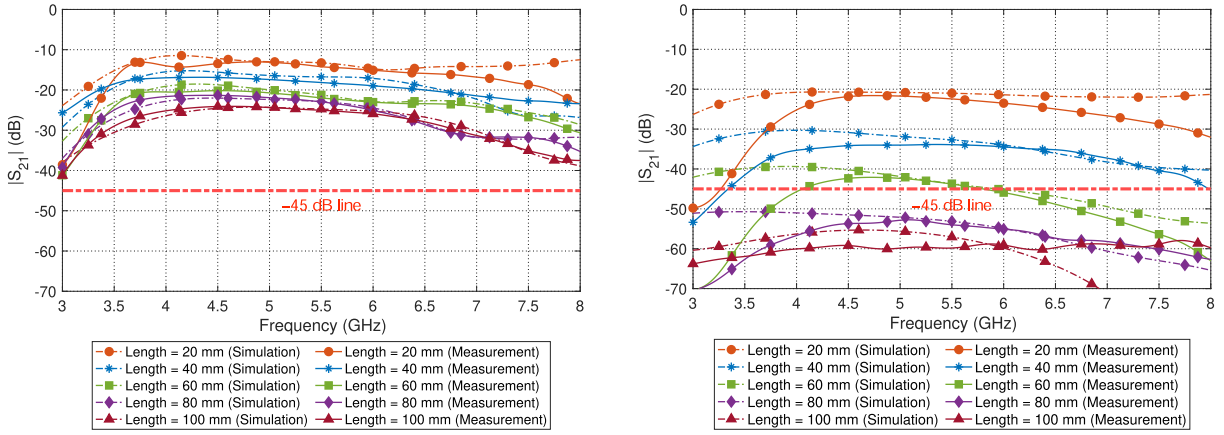

(a) Ex-vivo porcine tissue. **(b)** Tissue-equivalent phantom.

FIGURE 16. Type D: Transmission coefficient, $|S_{21}|$ dB.

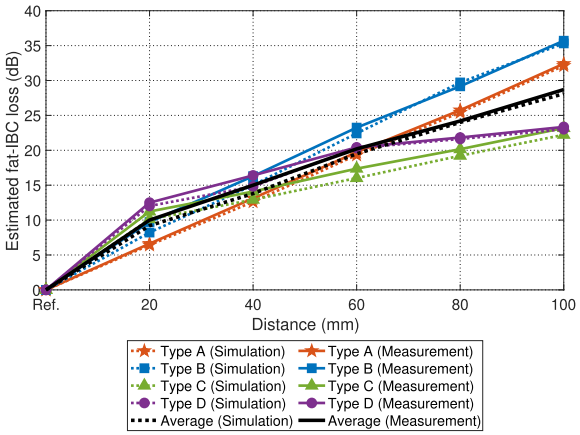

FIGURE 17. Path loss trend for the ex-vivo porcine tissue at 5.8 GHz.

Figure 13 shows the $|S_{21}|$ of Type A simulated and measured results for the ex-vivo and the phantom for different channel lengths. Figure 13a shows an excellent match between the simulated and measured $|S_{21}|$ results. Using the change in the $|S_{21}|$ values for different channel lengths, we estimate an average path loss of 6 dB/20 mm at 5.8 GHz. Since the loss tangent of the fat-equivalent phantom is twice that of the ex-vivo tissue, it was estimated that the average path loss is 12 dB/20 mm (see Figure 13b). In our measurements, we use a N9918A FieldFox Handheld Analyzer, which has a maximum dynamic range of –45 dBm across the frequency band of interest. In all figures, we plot the dash-dotted red line at –45 dB to mark the accuracy limit of the analyzer. As can be seen in Figures 13b–16b, the measurement data for 80 mm and 100 mm is almost flat over the entire band of interest. We therefore consider measurement results below –45 dB as faulty measurements and rely on the simulated results to draw our conclusions. Figure 14 shows the $|S_{21}|$ simulated and measured results for the ex-vivo and the phantom in the case of additional width in the fat transmission channel (Type B). Similar to Type A, the simulation and

TABLE 3. Simulated and measured transmission coefficient, $|S_{21}|$ for the different configuration types with respect to the channel length for ex-vivo porcine tissue at 5.8 GHz.

Types / Distance	Measured (Simulated), $\|S_{21}\|$ (dB)				
	20 mm	40 mm	60 mm	80 mm	100 mm
Type A	–8.8 (–8.4)	–15.3 (–14.6)	–21.9 (–21.3)	–27.9 (–27.4)	–34.6 (–34.1)
Type B	–11.9 (–10.2)	–18.5 (–17.0)	–25.5 (–24.4)	–31.4 (–31.7)	–37.9 (–37.3)
Type C	–13.4 (–12.1)	–16.3 (–14.9)	–19.6 (–18.0)	–22.4 (–21.2)	–25.4 (–24.2)
Type D	–14.7 (–14.0)	–18.6 (–16.8)	–22.6 (–22.3)	–24.0 (–23.6)	–25.6 (–25.0)

TABLE 4. Simulated and measured transmission coefficient, $|S_{21}|$ for the different configuration types with respect to the channel length for tissue-equivalent phantom at 5.8 GHz.

Types / Distance	Measured (Simulated), $\|S_{21}\|$ (dB)				
	20 mm	40 mm	60 mm	80 mm	100 mm
Type A	–16.2 (–15.5)	–30.1 (–28.6)	–44.2 (–43.1)	–55.8 (–53.1)	–58.9 (–75.0)
Type B	–18.2 (–17.5)	–32.2 (–31.4)	–46.3 (–45.3)	–59.2 (–59.9)	–59.4 (–67.9)
Type C	–20.5 (–19.8)	–31.0 (–29.3)	–41.7 (–39.8)	–54.1 (–53.0)	–56.0 (–51.6)
Type D	–22.3 (–21.2)	–34.2 (–33.4)	–45.0 (–44.6)	–54.6 (–54.1)	–58.9 (–58.5)

measurement results indicate an average channel path loss of almost 6 dB/20 mm, and the fat-equivalent phantom indicates 12 dB/20 mm.

Figure 15 shows the transmission coefficient of the Type C model, which has a thicker fat tissue. As can be seen in Figure 15a, at 100 mm distance, the signal coupling increased by more than 10 dB compared to Figures 13 and 14. Similarly, by comparing Type C results at 60 mm channel length, we note that there is an increase in the values of $|S_{21}|$ by 2.5 dB and 4.6 dB compared to Type A and Type B, respectively (see Figure 15b). Figure 16 shows the $|S_{21}|$ when the fat tissue is extended around the probes for both environments, ex-vivo porcine tissue and tissue-equivalent phantom. Type D, where the fat tissue surrounds the implant, is the case that mimics real-life scenarios most accurately. With the small probe size, we can easily implant the probe inside the fat tissue. Overall, we observed that Type C and D do not differ much in their signal transmission. This finding emphasizes that fat thickness has a significant influence on signal transmission. Figure 16a shows that the ex-vivo simulated and measured $|S_{21}|$ at 100 mm channel length is –25.6 dB and –25 dB, respectively. The simulated and measured $|S_{21}|$ for the phantom at 60 mm channel length is –45 dB and –44. dB, respectively (see Figure 16b).

Table 3 and 4 show a summary of the simulated and measured transmission coefficient $|S_{21}|$ for the different configuration types with respect to the channel length for ex-vivo porcine tissue and tissue-equivalent phantom at 5.8 GHz, respectively. Accordingly, we plot the values of the average path loss (excluding the probe-to-probe insertion loss of 2.2 dB), as shown in Figure 17. Figure 17 shows that the different environments have different path loss profiles.

Overall, our experiments show that Type C and D show lower signal path loss compared to Type A and B. The increase of the fat thickness in Type C and D explains the difference with respect to the other two types. The increase in the fat thickness decreases the path loss. We also observed that all measurement results are in good match with the simulation results. By considering the average for all distances, an estimated path loss per centimeter for the ex-vivo porcine tissue and tissue-equivalent phantom environments are shown as below. The bracketed values are the simulated results, and non-bracketed values are the measured results.

- Type A:
  –3.3 dB/cm (–3.2 dB/cm) for ex-vivo;
  –6.7 dB/cm (–6.8 dB/cm) for phantom.
- Type B:
  –4.0 dB/cm (–3.8 dB/cm) for ex-vivo;
  –7.1 dB/cm (–7.2 dB/cm) for phantom.
- Type C:
  –3.4 dB/cm (–3.1 dB/cm) for ex-vivo;
  –7.0 dB/cm (–6.7 dB/cm) for phantom.
- Type D:
  –3.8 dB/cm (–3.6 dB/cm) for ex-vivo;
  –7.5 dB/cm (–7.3 dB/cm) for phantom.

B. IMPACT OF NODE DISPLACEMENT

Figure 18 and 19 show the ex-vivo simulated results of the reflection coefficient $|S_{11}|$ and the transmission coefficient $|S_{21}|$ when the position of the transmitting probe is varied in the fat tissue as shown in Figure 12a. We note that the entire probe is surrounded by the fat tissue. The TX probe location is varied to study the impact on the signal coupling when nodes are misaligned/displaced in the fat channel medium. As a baseline for our experiments, we use the setup where the two probes are located in the center of the fat tissue.

Figure 18 summarizes the impact of the probes' vertical displacement on the signal coupling through the fat channel. Figure 18a shows that the displacement of the transmitting probe towards the skin (Up) or towards the muscle tissue (Down) has only a small impact on the probe's reflection coefficient $|S_{11}|$. Figure 18b shows that the displacement of the transmitting probe down towards the muscle leads to more loss compared to the displacement up towards the skin.

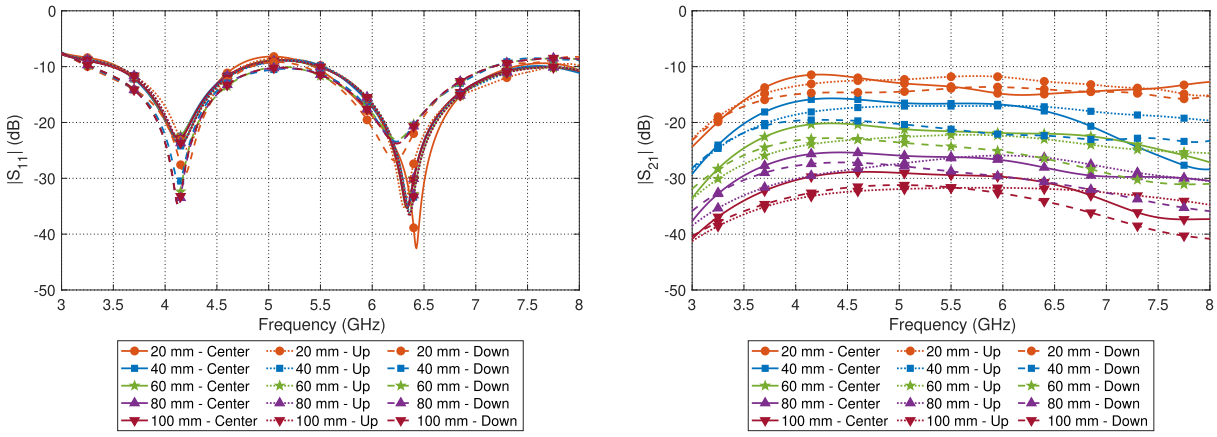

(a) Reflection coefficient, $|S_{11}|$. **(b)** Transmission coefficient, $|S_{21}|$.

FIGURE 18. Simulated results of $|S_{11}|$ and $|S_{21}|$ when the TX probe is placed in the center, below the skin, and on top of the muscle. The RX probe is placed in the center of the fat tissue.

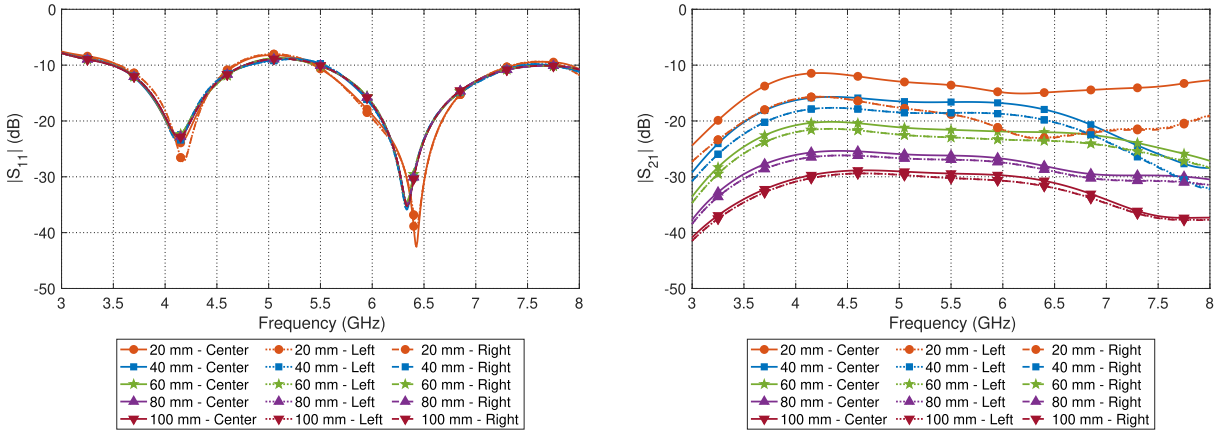

(a) Reflection coefficient, $|S_{11}|$. **(b)** Transmission coefficient, $|S_{21}|$.

FIGURE 19. Simulated results of $|S_{11}|$ and $|S_{21}|$ when TX probe is placed in the center, left side, and on the right side. The RX is placed in the center of the fat tissue.

Excluding the results of the 20 mm channel, we conclude that the vertical displacement of the probe increases the channel insertion loss by about 3 dB and 1 dB when the probe (node) is displaced down towards the muscle and up towards the skin tissues, respectively. The increase of the channel insertion loss as the probe is displaced down is attributed to the high losses caused by the muscle tissues near the probe channel interface.

Figure 19 summarizes the impact of the probe's horizontal displacement on the signal coupling through the fat channel. Figure 19a shows that the horizontal displacement has essentially no impact on the probe's reflection coefficient (excluding the minor changes for the 20 mm channel length). Moreover, the results of the transmission coefficient show that even at 15 mm horizontal displacement the insertion loss is increased by at most 2 dB compared to the baseline case. Note that the fat channel is horizontally symmetric, which is why the results of the right and left displacements in Figure 19 coincide.

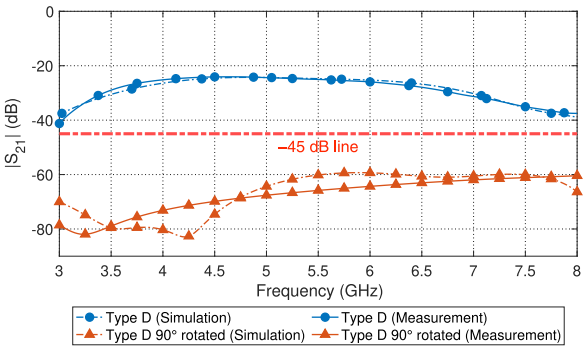

FIGURE 20. TX probe is 90° rotated for Type D: Transmission coefficient, $|S_{21}|$ dB for ex-vivo tissue.

C. WAVE POLARIZATION IMPACT

Figure 20 shows the impact on the signal coupling when the TX probe is rotated by 90° in ex-vivo porcine tissue. It can be seen that the $|S_{21}|$ drops by 35 dB and 38.4 dB with

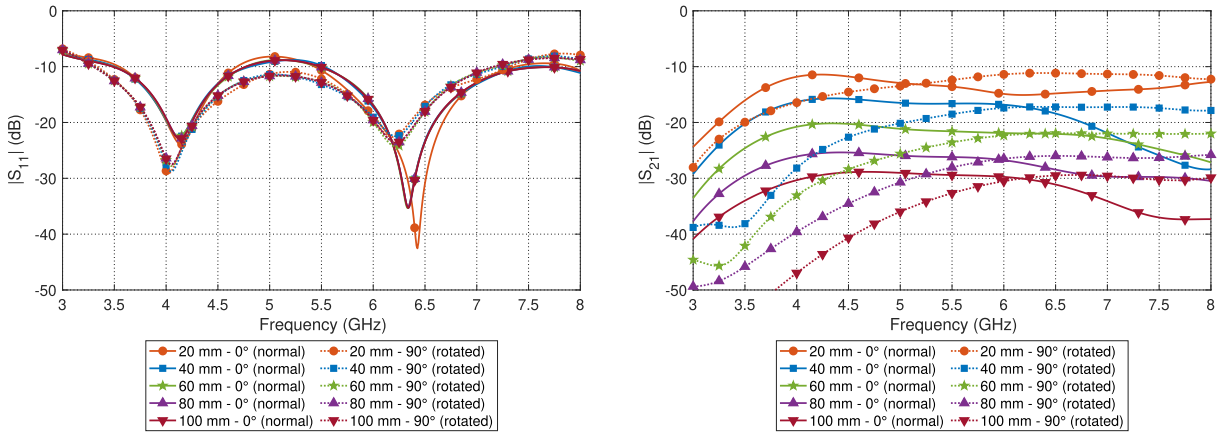

(a) Reflection coefficient, $|S_{11}|$. **(b)** Transmission coefficient, $|S_{21}|$.

FIGURE 21. Simulated results of $|S_{11}|$ and $|S_{21}|$ when TX and RX probes are at normal position (imposing vertical electric field) and 90° rotated (imposing horizontal electric field) in the channel.

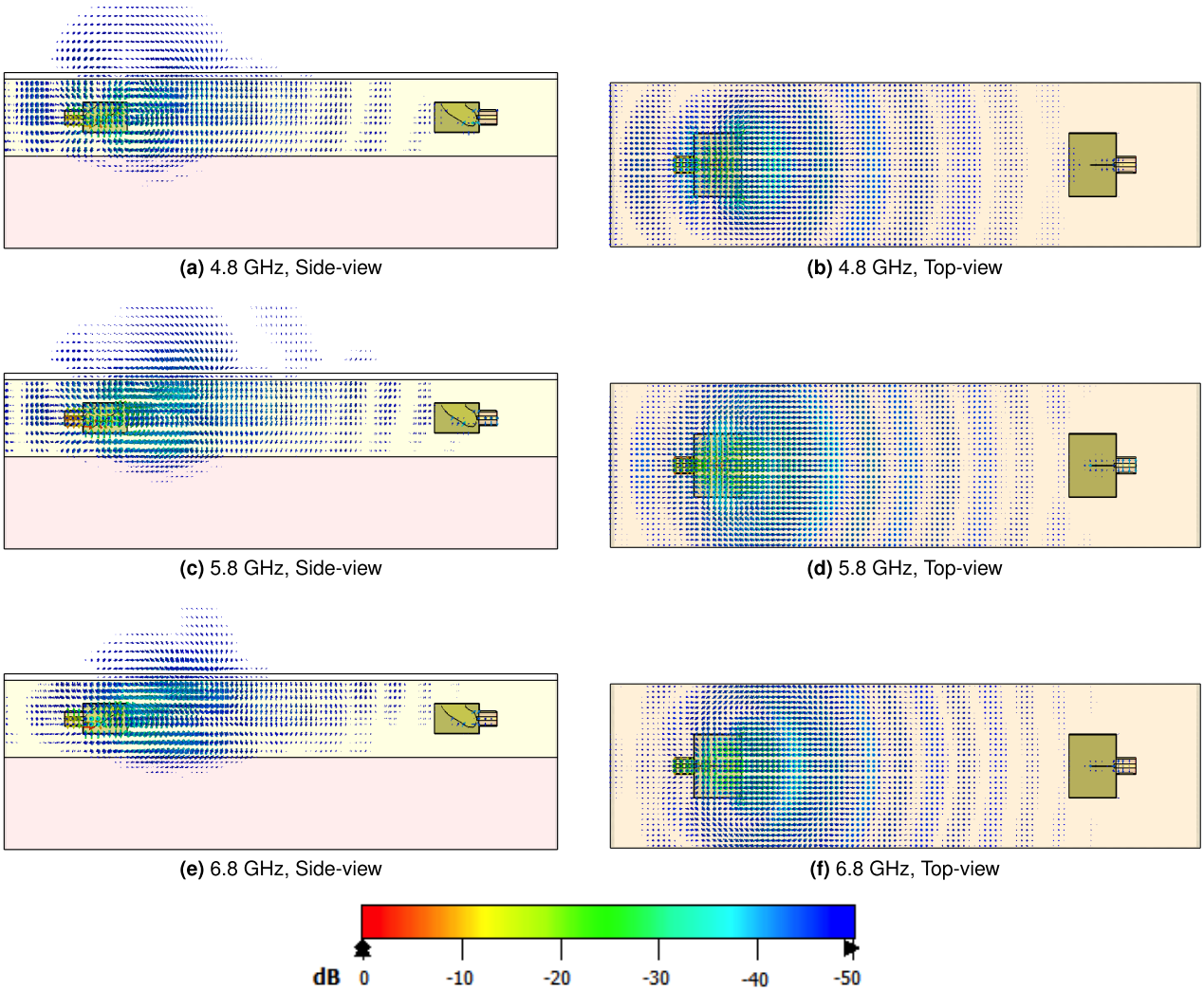

(a) 4.8 GHz, Side-view **(b)** 4.8 GHz, Top-view

(c) 5.8 GHz, Side-view **(d)** 5.8 GHz, Top-view

(e) 6.8 GHz, Side-view **(f)** 6.8 GHz, Top-view

FIGURE 22. The electric field distribution through the cross-section of the channel at 4.8 GHz, 5.8 GHz, and 6.8 GHz when TX and RX probes are at normal position (imposing vertical electric field) (a), (c), (e) Side-view; (b), (d), (f) Top-view, with scalar color map.

respect to the reference (Type D model) for the simulation and measurement, respectively, at 100 mm channel length.

To study the impact of imposing a horizontally polarized electric field into the fat channel, the two probes are

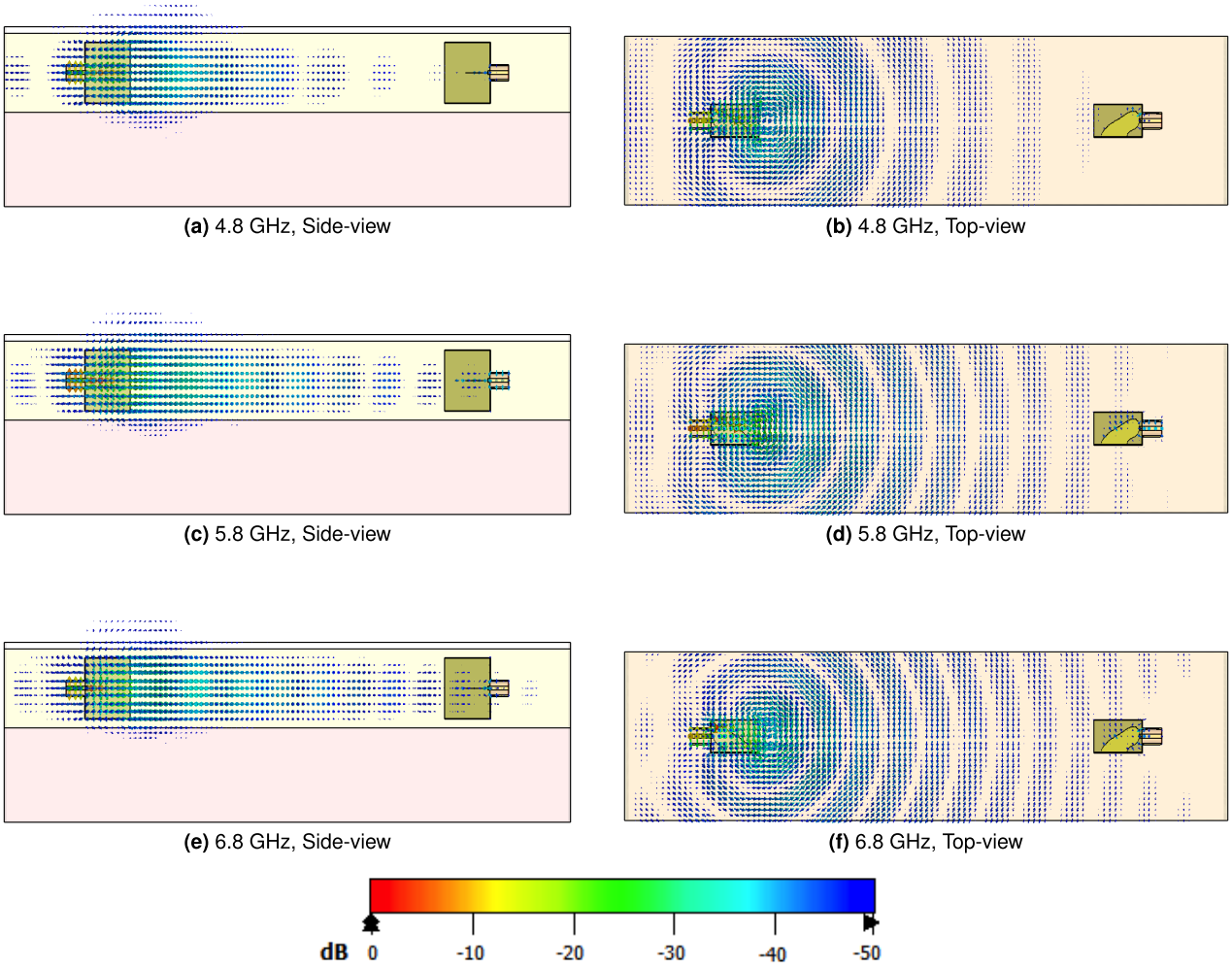

FIGURE 23. The electric field distribution through the cross-section of the channel at 4.8 GHz, 5.8 GHz, and 6.8 GHz when TX and RX probes are 90° rotated (imposing horizontal electric field) (a), (c), (e) Side-view; (b), (d), (f) Top-view, with scalar color map.

rotated. The analogy between the fat channel and parallel plate transmission line suggests that this horizontal electric field polarization is likely to excite the TE modes inside the fat channel [49]. Figure 21 shows a comparison between the performance of the fat channel for the two cases.

Similar to the case when the probe imposes a vertical polarized electric field, Figure 21a shows that the probe has a good matching to the fat channel. The $|S_{11}|$ is below –15 dB at 5.8 GHz. Figure 21b shows the results of $|S_{21}|$ when the distance between the TX and the RX varies from 20 mm to 100 mm. We note that the $|S_{21}|$ at 5.8 GHz do not vary much when the probes are rotated 90 degrees. In addition, we notice that the $|S_{21}|$ curve is essentially flat as the frequency increases. However towards higher frequencies, the case when both probes are rotated by 90° (horizontal electric field), the $|S_{21}|$ shows 5 dB better coupling compared to the normal position (vertical electric field). This observation suggests that fat-IBC can be further extended towards higher frequencies.

To investigate the near-field performance of the probe, we plot the electric field distribution when the probes are used to impose a vertical and a horizontal electric field into the fat channel, as shown in Figures 22 and 23, respectively. The figures demonstrate the performance of the probe around the 5.8 GHz and two additional plots for the 4.8 GHz and 6.8 GHz which reside at the edge of the F-band frequencies (4.9 GHz–7.05 GHz). Comparing the plots in both figures, we observe a higher signal amplitude for the 90° rotated case, both in the side-view and top-view for all frequencies, close to the receiver (RX) side. In addition, the comparison of the side-view in both figures shows that there is less leakage close to the transmitting (TX) probe for the case when the probes are 90° rotated.

VI. CONCLUSION

In this paper, we have investigated the fat-intrabody propagation channel at 5.8 GHz in the ISM band. The signal propagation setups were numerically modeled and developed

for six different types, including the effects of probe (node) displacement and a 90° rotation of the transmitter. The laboratory experiments were conducted in ex-vivo porcine and tissue-equivalent phantom environments. The scattering parameters were determined, and the path loss was estimated from the conducted measurements. The measurement results can be summarized as follows. Firstly, the path loss is dependent on the surrounding fat environment. In ex-vivo model, the increase in the fat thickness causes lower path loss in the channel transmission. Secondly, the change in the wave polarization between the transmitting and receiving nodes can have a severe negative impact on the signal coupling. In the extreme case when one of the node misaligned by 90°, this can reduce the received signal by around –38.4 dB (measurement) and –35 dB (simulation). Thirdly, the misalignment between two nodes inside the fat channel does not strongly affect the signal coupling, which is as low as 1 dB and 2 dB for both cases. The flat response of the transmission coefficient over a wide bandwidth suggests further investigations of the fat-IBC at even higher frequencies. Future research will include analytical channel modeling, studying the data-rate relation to the low and high frequencies, investigating realistic implant antennas, and more measurements for path loss analysis.

ACKNOWLEDGMENT

The computations were partially performed on resources provided by the Swedish National Infrastructure for Computing (SNIC) at the HPC2N Center.

REFERENCES

[1] U.S. Food & Drug Administration. *Wireless Medical Devices*. Accessed: Aug. 27, 2019. [Online]. Available: https://www.fda.gov/medical-devices/digital-health/wireless-medical-devices

[2] 2012. *Active Implantable Medical Devices—Electromagnetic Compatibility—EMC Test Protocols for Implantable Cardiac Pacemakers, Implantable Cardioverter Defibrillators and Cardiac Resynchronization Devices*. Accessed: Aug. 27, 2019. [Online]. Available: https://www.iso.org/standard/54472.html

[3] J. Gemio, J. Parron, and J. Soler, "Human body effects on implantable antennas for ISM bands applications: Models comparison and propagation losses study," *Prog. Electromagn. Res.*, vol. 110, pp. 437–452, Nov. 2010, doi: 10.2528/PIER10102604.

[4] *Remote-Controlled Drug Delivery Implant Size of Grape may Help Chronic Disease Management*, Houston Methodist, Houston, TX, USA, Sci. News, ScienceDaily, Jun. 2019.

[5] F. Robert, N. F. Sheppard, L. McCabe, R. M. Neer, J. M. Anderson, J. T. Santini, M. J. Cima, and R. Langer, "First-in-human testing of a wirelessly controlled drug delivery microchip," *Sci. Transl. Med.*, vol. 4, no. 122, p. 122, 2012, doi: 10.1126/scitranslmed.3003276.

[6] H. Gensler, R. Sheybani, P.-Y. Li, R. L. Mann, and E. Meng, "An implantable MEMS micropump system for drug delivery in small animals," *Biomed. Microdevices*, vol. 14, no. 3, pp. 483–496, Jun. 2012, doi: 10.1007/s10544-011-9625-4.

[7] M. Yip, R. Jin, H. H. Nakajima, K. M. Stankovic, and A. P. Chandrakasan, "A fully-implantable cochlear implant SoC with piezoelectric middle-ear sensor and arbitrary waveform neural stimulation," *IEEE J. Solid-State Circuits*, vol. 50, no. 1, pp. 214–229, Jan. 2015, doi: 10.1109/JSSC.2014.2355822.

[8] A. A. Eshraghi, R. Nazarian, F. F. Telischi, S. M. Rajguru, E. Truy, and C. Gupta, "The cochlear implant: Historical aspects and future prospects," *Anatomical Rec., Adv. Integr. Anatomy Evol. Biol.*, vol. 295, no. 11, pp. 1967–1980, Nov. 2012, doi: 10.1002/ar.22580.

[9] X. Meng, K. D. Browne, S.-M. Huang, C. Mietus, D. K. Cullen, M.-R. Tofighi, and A. Rosen, "Dynamic evaluation of a digital wireless intracranial pressure sensor for the assessment of traumatic brain injury in a swine model," *IEEE Trans. Microw. Theory Techn.*, vol. 61, no. 1, pp. 316–325, Jan. 2013, doi: 10.1109/TMTT.2012.2224361.

[10] U. Kawoos, X. Meng, M.-R. Tofighi, and A. Rosen, "Too much pressure: Wireless intracranial pressure monitoring and its application in traumatic brain injuries," *IEEE Microw. Mag.*, vol. 16, no. 2, pp. 39–53, Mar. 2015, doi: 10.1109/MMM.2014.2377585.

[11] X. Meng, U. Kawoos, S.-M. Huang, M.-R. Tofighi, and A. Rosen, "Implantable wireless devices for the monitoring of intracranial pressure," in *Proc. IEEE 16th Int. Symp. Consum. Electron.*, Harrisburg, PA, USA, Jun. 2012, pp. 1–2, doi: 10.1109/ISCE.2012.6241727.

[12] L. Marnat, M. H. Ouda, M. Arsalan, K. Salama, and A. Shamim, "On-chip implantable antennas for Wireless power and data transfer in a glaucoma-monitoring SoC," *IEEE Antennas Wireless Propag. Lett.*, vol. 11, pp. 1671–1674, 2012, doi: 10.1109/LAWP.2013.2240253.

[13] A. Koutsonas, P. Walter, G. Roessler, and N. Plange, "Implantation of a novel telemetric intraocular pressure sensor in patients with glaucoma (ARGOS Study): 1-year results," *Investigative Ophthalmol. Vis. Sci.*, vol. 56, no. 2, pp. 1063–1069, Feb. 2015, doi: 10.1167/iovs.14-14925.

[14] P. F. Pasquina, M. Evangelista, A. J. Carvalho, J. Lockhart, S. Griffin, G. Nanos, P. McKay, M. Hansen, D. Ipsen, J. Vandersea, J. Butkus, M. Miller, I. Murphy, and D. Hankin, "First-in-man demonstration of a fully implanted myoelectric sensors system to control an advanced electromechanical prosthetic hand," *J. Neurosci. Methods*, vol. 244, pp. 85–93, Apr. 2015, doi: 10.1016/j.jneumeth.2014.07.016.

[15] E. Mastinu, P. Doguet, Y. Botquin, B. Hakansson, and M. Ortiz-Catalan, "Embedded system for prosthetic control using implanted neuromuscular interfaces accessed via an osseointegrated implant," *IEEE Trans. Biomed. Circuits Syst.*, vol. 11, no. 4, pp. 867–877, Aug. 2017, doi: 10.1109/TBCAS.2017.2694710.

[16] D. McDonnall, S. Hiatt, C. Smith, and K. S. Guillory, "Implantable multichannel wireless electromyography for prosthesis control," in *Proc. Annu. Int. Conf. IEEE Eng. Med. Biol. Soc.*, San Diego, CA, USA, Aug. 2012, pp. 1350–1353, doi: 10.1109/EMBC.2012.6346188.

[17] D. D. Karnaushenko, D. Karnaushenko, D. Makarov, and O. G. Schmidt, "Compact helical antenna for smart implant applications," *NPG Asia Mater.*, vol. 7, no. 6, p. e188, Jun. 2015, doi: 10.1038/am.2015.53.

[18] D. G. Rucker, H. R. Khaleel, S. S. Raheem, and H. M. Al-Rizzo, "Microstrip antenna arrays for implantable and wearable wireless applications," in *Wireless Mobile Communication and Healthcare* (Lecture Notes of the Institute for Computer Sciences, Social Informatics and Telecommunications), vol. 55, J. C. Lin and K. S. Nikita, Eds. Berlin, Germany: Springer, 2011, pp. 135–143, doi: 10.1007/978-3-642-20865-2_18.

[19] B. T. Nukala, J. Tsay, D. Y. C. Lie, J. Lopez, and T. Q. Nguyen, "Efficient near-field inductive wireless power transfer for miniature implanted devices using strongly coupled magnetic resonance at 5.8 GHz," in *Proc. Texas Symp. Wireless Microw. Circuits Syst. (WMCS)*, Waco, TX, USA, Mar. 2016, pp. 1–4, doi: 10.1109/WMCaS.2016.7577481.

[20] Y. Chan, M. Q.-H. Meng, K.-L. Wu, and X. Wang, "Experimental study of radiation efficiency from an ingested source inside a human body model*," in *Proc. IEEE Eng. Med. Biol. 27th Annu. Conf.*, Shanghai, China, 2005, pp. 7754–7757, doi: 10.1109/IEMBS.2005.1616310.

[21] M. R. Basar, F. Malek, K. M. Juni, M. S. Idris, and M. I. M. Saleh, "Ingestible wireless capsule technology: A review of development and future indication," *Int. J. Antennas Propag.*, vol. 2012, pp. 1–14, Dec. 2012, doi: 10.1155/2012/807165.

[22] N. B. Asan, D. Noreland, E. Hassan, S. R. M. Shah, A. Rydberg, T. J. Blokhuis, P.-O. Carlsson, T. Voigt, and R. Augustine, "Intra-body microwave communication through adipose tissue," *Healthcare Technol. Lett.*, vol. 4, no. 4, pp. 21–115, Aug. 2017, doi: 10.1049/htl.2016.0104.

[23] N. Asan, E. Hassan, J. Shah, D. Noreland, T. Blokhuis, E. Wadbro, M. Berggren, T. Voigt, and R. Augustine, "Characterization of the fat channel for intra-body communication at R-band frequencies," *Sensors*, vol. 18, no. 9, p. 2752, Aug. 2018, doi: 10.3390/s18092752.

[24] N. B. Asan, C. P. Penichet, S. R. M. Shah, D. Noreland, E. Hassan, A. Rydberg, T. J. Blokhuis, T. Voigt, and R. Augustine, "Data packet transmission through fat tissue for wireless IntraBody networks," *IEEE J. Electromagn., RF Microw. Med. Biol.*, vol. 1, no. 2, pp. 43–51, Dec. 2017, doi: 10.1109/JERM.2017.2766561.

[25] N. B. Asan, J. Velander, Y. Redzwan, R. Augustine, E. Hassan, D. Noreland, T. Voigt, and T. J. Blokhuis, "Reliability of the fat tissue channel for intra-body microwave communication," in *Proc. IEEE Conf. Antenna Meas. Appl. (CAMA)*, Tsukuba, Japan, Dec. 2017, pp. 310–313, doi: 10.1109/CAMA.2017.8273435.
[26] N. B. Asan, J. Velander, S. Redzwan, M. Perez, E. Hassan, T. J. Blokhuis, T. Voigt, and R. Augustine, "Effect of thickness inhomogeneity in fat tissue on in-body microwave propagation," in *Proc. IEEE Int. Microw. Biomed. Conf. (IMBioC)*, Philadelphia, PA, USA, Jun. 2018, pp. 136–138, doi: 10.1109/IMBIOC.2018.8428872.
[27] N. B. Asan, E. Hassan, M. D. Perez, S. R. M. Shah, J. Velander, T. J. Blokhuis, T. Voigt, and R. Augustine, "Assessment of blood vessel effect on fat-intrabody communication using numerical and *ex-vivo* models at 2.45 GHz," *IEEE Access*, vol. 7, pp. 89886–89900, 2019, doi: 10.1109/ACCESS.2019.2926646.
[28] M. SarestoNiemi, C. Pomalaza-raez, Z. Bi, T. Kumpuniemi, C. Kissi, M. Sonkki, M. Hamalainen, and J. Iinattit, "Comprehensive study on the impact of sternotomy wires on UWB WBAN channel characteristics on the human chest area," *IEEE Access*, vol. 7, pp. 74670–74682, 2019, doi: 10.1109/ACCESS.2019.2920067.
[29] M. Sarestoniemi, C. Pomalaza-Raez, C. Kissi, M. Berg, M. Hamalainen, and J. Iinatti, "WBAN channel characteristics between capsule endoscope and receiving directive UWB on-body antennas," *IEEE Access*, vol. 8, pp. 55953–55968, 2020, doi: 10.1109/ACCESS.2020.2982247.
[30] D. Andreuccetti, "An Internet resource for the calculation of the dielectric properties of body tissues in the frequency range 10 Hz–100 GHz," in *Proc. IFAC-CNR*, Florence, Italy, 1997. Accessed: Mar. 23, 2021. [Online]. Available: https://niremf.ifac.cnr.it/tissprop/
[31] S. Gabriel, R. W. Lau, and C. Gabriel, "The dielectric properties of biological tissues: II. Measurements in the frequency range 10 Hz to 20 GHz," *Phys. Med. Biol.*, vol. 41, no. 11, pp. 2251–2269, Nov. 1996.
[32] S. Gabriel, R. W. Lau, and C. Gabriel, "The dielectric properties of biological tissues: III. Parametric models for the dielectric spectrum of tissues," *Phys. Med. Biol.*, vol. 41, no. 11, pp. 2271–2293, Nov. 1996.
[33] L. Joseph, N. B. Asan, J. Ebrahimizadeh, A. S. Chezhian, M. D. Perez, T. Voigt, and R. Augustine, "Non-invasive transmission based tumor detection using anthropomorphic breast phantom at 2.45 GHz," in *Proc. 14th Eur. Conf. Antennas Propag. (EuCAP)*, Copenhagen, Denmark, Mar. 2020, pp. 1–5, doi: 10.23919/EuCAP48036.2020.9135953.
[34] 2018. *Keysight N1501A Dielectric Probe Kit 10 MHz to 50 GHz*. Keysight Technologies. Accessed: Aug. 27, 2019. [Online]. Available: https://literature.cdn.keysight.com/litweb/pdf/5992-0264EN.pdf
[35] C. Gabriel and A. Peyman, "Dielectric measurement: Error analysis and assessment of uncertainty," *Phys. Med. Biol.*, vol. 51, no. 23, pp. 6033–6046, Dec. 2006.
[36] E. Hassan, D. Noreland, E. Wadbro, and M. Berggren, "Topology optimisation of wideband coaxial-to-waveguide transitions," *Sci. Rep.*, vol. 7, no. 1, p. 45110, Apr. 2017, doi: 10.1038/srep45110.
[37] A. Taflove and S. Hagness, *Computational Electrodynamics: The Finite-Difference Time-Domain Method*, 3rd ed. Norwood, MA, USA: Artech House, 2005.
[38] E. Hassan, E. Wadbro, and M. Berggren, "Topology optimization of metallic antennas," *IEEE Trans. Antennas Propag.*, vol. 62, no. 5, pp. 2488–2500, May 2014.
[39] E. Hassan, E. Wadbro, and M. Berggren, "Time-domain sensitivity analysis for conductivity distribution in Maxwell's equations," Dept. of Comput. Sci., Umeå Univ., Umeå, Sweden, Tech. Rep. UMINF 15.06, 2015.
[40] K. Svanberg, "A class of globally convergent optimization methods based on conservative convex separable approximations," *SIAM J. Optim.*, vol. 12, no. 2, pp. 555–573, Jan. 2002.
[41] E. Hassan, B. Scheiner, F. Michler, M. Berggren, E. Wadbro, F. Rohrl, S. Zorn, R. Weigel, and F. Lurz, "Multilayer topology optimization of wideband SIW-to-waveguide transitions," *IEEE Trans. Microw. Theory Techn.*, vol. 68, no. 4, pp. 1326–1339, Apr. 2020.
[42] CST STUDIO SUITE. *BS Dassault Systèmes*. Accessed: Mar. 23, 2021. [Online]. Available: https://www.3ds.com/products-services/simulia/products/cst-studio-suite/
[43] T. Tuovinen, K. Y. Yazdandoost, and J. Iinatti, "Comparison of the performance of the two different UWB antennas for the use in WBAN on-body communication," in *Proc. 6th Eur. Conf. Antennas Propag. (EUCAP)*, Prague, Czech Republic, Mar. 2012, pp. 2271–3374, doi: 10.1109/EuCAP.2012.6206090.
[44] C. Kissi, M. Särestöniemi, C. Pomalaza-Ráez, M. Sonkki, and M. N. Srifi, "Low-UWB directive antenna for wireless capsule endoscopy localization," in *13th EAI International Conference on Body Area Networks* (EAI Innovations in Communication and Computing), C. Sugimoto, H. Farhadi, and M. Hämäläinen, Eds. Cham, Switzerland: Springer, 2020, doi: 10.1007/978-3-030-29897-5_38.
[45] 2018. *FieldFox Handheld Analyzers Data Sheet*. Keysight Technologies. Accessed: Aug. 27, 2019. [Online]. Available: https://literature.cdn.keysight.com/litweb/pdf/5990-9783EN.pdf
[46] M. A. Gibney, C. H. Arce, K. J. Byron, and L. J. Hirsch, "Skin and subcutaneous adipose layer thickness in adults with diabetes at sites used for insulin injections: Implications for needle length recommendations," *Current Med. Res. Opinion*, vol. 26, no. 6, pp. 1519–1530, Jun. 2010, doi: 10.1185/03007995.2010.481203.
[47] C. W. Kim and T. S. P. See, "RF transmission power loss variation with abdominal tissues thicknesses for ingestible source," in *Proc. IEEE 13th Int. Conf. e-Health Netw., Appl. Services*, Columbia, MO, USA, Jun. 2011, pp. 282–287, doi: 10.1109/HEALTH.2011.6026766.
[48] C. Gabriel and S. Gabriel, "Compilation of the dielectric properties of body tissues at RF and microwave frequencies," in *Proc. IFAC-CNR*, Florence, Italy, 1997. Accessed: Mar. 23, 2021. [Online]. Available: https://niremf.ifac.cnr.it/docs/DIELECTRIC/Report.html
[49] D. M. Pozar, "Transmission lines and waveguides," in *Microwave Engineering*, 4th ed. Hoboken, NJ, USA: Wiley, 2012, pp. 102–110.

NOOR BADARIAH ASAN (Member, IEEE) received the B.Eng. degree in electronic engineering (telecommunication electronics) from Universiti Teknikal Malaysia Melaka, Malaysia, in 2008, the M.Eng. degree in communication and computer from Universiti Kebangsaan Malaysia, in 2012, and the Ph.D. degree in engineering science with specialization in microwave technology from Uppsala University, in November 2019. She joined the Department of Electronics and Computer Engineering, Universiti Teknikal Malaysia Melaka, as a Tutor Lecturer in 2009, where she was appointed as a Lecturer in 2012 and a Senior Lecturer in 2021. She is currently a Senior Lecturer with the Universiti Teknikal Malaysia Melaka. Her current research interests include the design of small antennas (on-body), implant antennas (in-body), microwave sensors, EM-based computer-aided antenna design, intrabody wireless sensor networks, microwave material characterization, and design, optimize, and characterize biomedical sensor in fat-intrabody microwave communication (fat-IBC), and biomedical application.

EMADELDEEN HASSAN received the B.Sc. and M.Sc. degrees in electronics and communication engineering from Menoufia University, Menouf, Egypt, in 2001 and 2006, respectively, and the Licentiate and Ph.D. degrees in computational science and engineering from Umeå University, Umeå, Sweden, in 2013 and 2015, respectively. From 2017 to 2018, he was a Postdoctoral Fellow with the Department of Computing Science, Umeå University. In 2018, he was the Guest Scientist of the Institute for Electronics Engineering, Friedrich-Alexander University, Erlangen, Germany. Since 2021, he has been an Associate Professor with the Department of Applied Physics and Electronics Umeå University. His research interests include numerical methods in electromagnetics (EM), antenna design optimization, waveguides' transitions optimization, medical applications of EM, electromagnetic band gap structures (EBG), and nondestructive evaluation and testing, optimization methods, and parallel programming.

MAURICIO DAVID PEREZ (Member, IEEE) received the Engineering degree in electronics from the National Technological University (UTN), Argentina, in 2007, and the Ph.D. degree in electrical engineering from the University of Bologna, Italy, in 2012. He has worked as an Industrial Researcher in Italy, from 2012 to 2014, and an Academic Teacher and a Researcher with UTN, from 2014 to 2017. He is currently a Teacher and a Researcher with the Ångström Laboratories, Microwaves in Medical Engineering Group (MMG), Uppsala University, Sweden. His research interest includes modeling and data-driven validation of microwave sensors for biomedical applications.

LAYA JOSEPH received the Engineering degree in electronics and communication from Calicut University, India, in 2009, and the master's degree in engineering physics from Uppsala University, Sweden, in 2019. She has worked as a Research Engineer with the Micro Structure Technology (MST) Division and the Ångström Laboratory, Solid State Electronics Division, Microwaves in Medical Engineering Group (MMG), Uppsala University, from 2019 to 2020. Her research interests include biological microwave phantoms for intrabody communication, breast tumor sensing, and stretchable printed circuit boards for skin worn wireless networks.

MARTIN BERGGREN received the Ph.D. degree in computational and applied mathematics from Rice University, Houston, TX, USA, in 1996. He is currently a Professor of scientific computing with Umeå University, Umeå, Sweden. Previously, he held a lectureship position at Uppsala University, Uppsala, Sweden, and research positions at the Swedish Defence Research Agency, Stockholm, Sweden, and Sandia National Laboratories, Albuquerque, NM, USA. His research interests include numerical methods for partial differential equations, and, in particular, computational design optimization for acoustic and electromagnetic wave propagation problems.

THIEMO VOIGT (Member, IEEE) received the Ph.D. degree from Uppsala University, Sweden, in 2002. He is currently a Professor of computer science with the Department of Information Technology, Uppsala University. He also leads the Networked Embedded Systems Group, RISE Computer Science. His current research interests include system software for embedded networked devices and the Internet of Things. His work has been cited more than 14 500 times. He is a member of the editorial board for the IEEE INTERNET OF THINGS and *ACM Transactions on Sensor Networks* (TOSN).

ROBIN AUGUSTINE (Member, IEEE) graduated in electronics science from Mahatma Gandhi University, India, in 2003. He received the master's degree in robotics from the Cochin University of Science and Technology, India, in 2005, and the Ph.D. degree in electronics and optic systems from Université Paris Est Marne La Vallée, France, in July 2009. He was a Postdoctoral Fellow with IETR, University of Rennes 1, Rennes, France, from 2009 to 2011. He joined Uppsala University as a Senior Researcher in 2011. He became a Docent in Microwave Technology in 2016 and a University Lecturer (an Associate Professor) in medical engineering in 2020. He is currently an Associate Professor with the Division of Solid-State Electronics Specialized in Microwave Technology and Medical Engineering. Since 2015, he has been the Head of the Microwaves in Medical Engineering Group (MMG) consisting of 16 members. MMG has five researchers, two Ph.D. students, three research engineers, and six interns. He is the author or a coauthor of more than 150 publications, including journals and conferences. His current research interests include the designing of wearable antennas, BMD sensors, dielectric characterization, bio-electromagnetics, non-invasive diagnostics, fat-intrabody communication, microwave phantoms, biological effects of millimeter waves, RF backscattering, NDEs, and RF in MRI, with an emphasis on *in vitro* studies. He has received Carl Trygger and Olle Engqvist Fundings for Postdoctoral studies. He is a regular convened Session Organizer in EuCAP since 2016. He is also the PI of the Indo-Swedish Vinnova Project BDAS and for Swedish part of the bilateral (Holland and Sweden) Horizon 2020 Eurostars Project COMFORT. In February 2016, he became a Docent (an Associate Professor) at UU. He was a recipient of prestigious Vetenskapsrådet (VR) Project Grant 2017 for his project on a novel modality for Osteodiagnosis. He was a recipient of the UGCRFSMS Fellowship for meritorious students from Indian Government and the EGIDE Eiffel Grant for Excellence from French Research Ministry, in 2006 and 2008, respectively. He is a WPL of the EU Project SINTEC, SSF Framework Grant LifeSec, and Vinnova Grant "connect my body," in 2018. He is the Research Lead for the Eurostars projects SenseBurn 2018 and MAS 2020. He is also the Founder, the CTO, and the Chairman of Probingon AB specializing in point of care sensors.